ORIGINAL RESEARCH ARTICLE

Laser Welding of Nitinol Thin Foils: Mechanical Properties and Microstructure Depending on Process Parameters

D. KATRAKOVA-KRÜGER, L. PEGORARO, L. SALMASO, C. HARTL, I. SCHULZ, S. WEICHERT, and R. STEFFEN

Ni–Ti alloys are used as functional materials in numerous sectors such as aerospace, automotive engineering, medical technology, and consumer goods. Their properties in terms of shape memory effect and superelasticity offer a great potential for innovative smart products. However, forming and machining of these alloys into concrete products is challenging. Assembling plain structures by laser welding to complex product shapes offers an economical alternative in many cases, but can be associated with negative effects, such as reduction of strength, development of brittle intermetallic compounds, alteration of transformation temperatures, and modification of shape memory effects and superelastic behavior. Against this background, investigations on laser welding of Ni55/Ti45 foil with a thickness of 125 μm by a fiber laser were conducted. Supported by methods of design of experiments, optimal parameters were determined with respect to laser power, welding speed, focus position, and beam oscillation, and the welding results were analyzed concerning the microstructure and mechanical characteristics of the welded joints. The effect of laser beam oscillation was investigated for the first time for the welding of this alloy. Due to the very low thickness, the preparation of the foils for the microstructure characterization is quite demanding. Best results were obtained by ion milling. Fracture surfaces and the influence of the welding were also investigated.

https://doi.org/10.1007/s11661-022-06954-1

I. INTRODUCTION

AMONG the shape memory alloys (SMA), Ni–Ti alloys are one of the most important and most frequently used alloys due to their distinctive properties with regard to the shape memory effect and superelasticity.[1] Examples of innovative applications of Ni–Ti-based SMA can be found in the areas of biomedical applications, automotive engineering, aerospace technology, structural engineering, marine technology, actuator technology, robots, microfluidics, micro-electromechanical systems, and heat engines.[2–11] Although it should be mentioned that due to recent developments in the area of the less expensive iron-based and copper-based SMA, potential alternatives to Ni–Ti alloys with regard to these properties have emerged[12,13] and in the case of a Cu–Al–Be SMA successful laser welding has already been demonstrated.[14] The fabrication of specific products made from Ni–Ti alloys by processes such as machining, casting, and metal forming poses challenges due to the difficult processability of these alloys,[15–18] which limits possible innovative applications. It must be pointed out, however, that promising progress has been made in the field of additive manufacturing of Ni–Ti alloys, *e.g.*, for wire-based additive techniques such as electron-beam free forming and ultra-high-frequency pulsed gas tungsten arc welding, which has led to improved process understanding[19,20] and new strategies for components with outstanding properties.[21] Although these additive processes already enable high building speeds and comparatively large workpieces, challenges for the application of additive manufacturing processes with

D. KATRAKOVA-KRÜGER, I. SCHULZ, and S. WEICHERT are with the Materials Laboratory, TH Köln, Steinmüllerallee 1, 51643 Gummersbach, Germany. Contact e-mail: danka.katrakova-krueger@th-koeln.de L. PEGORARO and L. SALMASO are with the Department of Management and Engineering, University of Padua, Stradella S. Nicola, 3, 36100 Vicenza, Italy. C. HARTL is with the Faculty of Automotive Engineering and Production, TH Köln, Betzdorfer Str. 2., 50679 Cologne, Germany. R. STEFFEN is with the Hitachi High-Tech Europe GmbH, Europark Fichtenhain A12, 47807 Krefeld, Germany.
Manuscript submitted December 11, 2022; accepted December 26, 2022.
Article published online January 24, 2023

Ni–Ti alloys still consist in anisotropy, very thin cross sections, surface quality, and costs. Assembling plain structures by welding to required complex product shapes can therefore still offer an economical alternative in many cases. Among available conventional welding technologies, laser welding is reported as the most employed and studied technique for shape memory alloys, also because of its high energy density that supports a low heat-affected zone around the weld seam.[15,22,23] For welding structures in the micro range, such as thin foils, which is the focus of the present work, fiber lasers and Nd:YAG lasers show advantages for welding of Ni–Ti alloys over CO_2 lasers in terms of the smaller heat-affected zone and higher energy absorption due to the shorter wavelength.[24,25] In the sense of the definition of meso and micro dimensions of components according to Reference 26 thin foils are understood in this work as foils with thicknesses in the sub-millimeter/micro-meter range.

Although numerous studies exist on laser welding of Ni–Ti alloys as for example summarized in References 23, 25, the studies on welding thin foils among them are rather limited, as of interest for example for reconfigurable systems such as mobile phone antennas or temperature-sensitive actuators.[27,28] Chan *et al.*[29] investigated the welding of foils with a thickness of 250 μm made from a Ni–Ti alloy with 55.91 wt pct of Ti using a continuous wave fiber laser with a nominal power of 100 W, obtaining welds that were mainly of cellular dendrites and with a small amount of Ni_3Ti as a brittle intermetallic phase. Also, it was found that the onset of austenite and martensite start temperatures, A_s and M_s, of the Ni–Ti welds shifted to lower values as compared to the as-received Ni–Ti alloy.[29] Khan *et al.*[30] studied the effects of process parameters on the mechanical and pseudoelastic properties of a Ni-rich alloy with 55.8 wt pct of Ni on the welding of foils with 370 μm thickness using a pulsed Nd:YAG laser and observed noteworthy influences of laser parameters on the welded material properties. Oliveira *et al.*[31] carried out investigations into the mechanisms responsible for the existence of martensite at room temperature after laser welding sheets with a thickness of 1000 μm of an austenitic Ni–Ti alloy with 50.8 at. pct of Ni applying a Nd:YAG laser. Martensite was detected in the heat-affected zone (HAZ) as well as in the fusion zone (FZ) and the occurrence of precipitations (Ni_4Ti_3) in the HAZ was discussed.[31] Welding of Ni–Ti sheets made from an alloy with 52 at. pct of Ni and the thickness of 1000 μm was examined by Datta *et al.*[22] using a 2000 W fiber laser. Intermetallic phases, such as Ni_3Ti and Ti_2Ni, were observed in the welded zone and were related to the drastically reduced strength and elongation at fracture of the joint along with microstructural changes due to the welding.[22]

The published scientific papers on laser welding of Ni–Ti alloy sheets and foils typically considered the influences of laser power and welding speed on the welding result, and in some cases also the influence of the focus position, as in Reference 24. So far, the effect of the superposition of an oscillating movement of the laser beam transverse to the welding direction has not been investigated for laser welding of Ni–Ti materials to the knowledge of the authors. For the laser welding of high-strength steel Chen *et al.*[32] found that the laser beam oscillation was beneficial to improve the microstructure compared to welding without oscillation. The latter led to mainly coarse columnar grains while superimposed oscillation resulted in refined columnar grains with equiaxed grains in the weld center and higher tensile strengths of the weld.[32] The effect of a S-curve laser power for power distribution control on laser oscillating welding of an aluminum alloy was investigated by Tan *et al.*[33] With this strategy, a refined grain structure, a narrowed columnar region, and improved mechanical properties of the joints were achieved, with the S-curve power providing higher tensile strengths compared to the process with constant power.[33] Wang *et al.*[34] observed that an oscillation increases the stirring effect of the molten metal pool and found that oscillation mitigates macrosegregation of the weld for the laser-arc hybrid welding of aluminum. For laser welding of a Fe–Ni–Co superalloy Hu *et al.*[35] determined that the laser beam oscillation inhibits pores, spatters, and cracks and increases tensile strength and elongation at break within the welded joints. Based on a developed multi-physics model, Ke *et al.*[36] investigated the key-hole-induced porosity formation during laser welding of an aluminum alloy without and with different forms of oscillation and parameters for the suppression of pores could be found. The influence of different forms of oscillation has also been studied experimentally by Zhou *et al.*[37] for the welding of an Al–Li alloy with the result that oscillation brings visible improvements in the collapse of the weld, increase in tensile strength, and refinement of the grain structure in the weld, with varying results for the different forms of oscillation. The feasibility to bridge gaps along the weld seam and the influence on residual stresses and fatigue strength with laser beam oscillation and defocused beam was studied by Hensel *et al.*[38]

In summary, the welding of thin Ni–Ti foils, which is of interest for new innovative products, shows specific difficulties but for welding the materials investigated in the literature, the application of an oscillating motion superimposed on the laser beam movement has provided a number of advantages for the weld quality. For the Ni–Ti material in the foreground here, however, it has not yet been researched how the application of oscillation affects the welding result. In the event that oscillation is associated with a higher heat input, for example, a deterioration in the mechanical behavior especially for high strain and long duration cyclic load is probable.[39] Against this background, the present study investigated the butt welding of Ni–Ti foils with a thickness of 125 μm using a fiber laser with orbital beam oscillation. The focus was on the strength of the welded joint, the resulting microstructure, and the formation of the fracture surface of the tested specimens.

II. MATERIALS AND METHODS

Samples from Ni–Ti foils were butt welded with selected parameters and analyzed with respect to mechanical properties and the microstructure using ion milling (IM) technology for sample preparation. The applied welding parameters were developed with the support of methods of Design of Experiments (DoE) as an optimal welding parameter set in terms of joint strength. This parameter set contained a superimposed oscillation of the laser beam. The results obtained with these welding parameters were compared with welding results of a second parameter set for a linear movement of the laser beam. The following sections describe the methods of the individual investigation steps.

A. *Laser Welding Process*

Laser welding was conducted with an ytterbium fiber laser of the type YLR-50-SM (manufacturer: IPG Laser), providing a beam with a wavelength of 1070 nm and a maximum power of 50 W in CW mode with a focal spot diameter of 32 μm. For specimen fabrication, rectangular strips were first cut out of the foil by wire electrical discharge machining (EDM), cleaned and degreased and then welded. For the welding process, the specimens were clamped in a fixture and butt welded under an inert argon gas atmosphere, Figure 1.

The movement of the laser beam along the weld seam was realized by a galvanometer scanner equipped with controllable deflection mirrors, which also enabled an oscillation of the beam, Figure 2. A circular oscillation was chosen in the investigations presented here. The final specimen geometry for tensile tests according to Figure 3 was created then from the welded strips by laser cutting, which also served to eliminate the typically uneven start and end of the welding seam.

The selected process parameters to fabricate the welded specimens in terms of laser power P, welding speed v, focus position z_f, amplitude A and frequency f of the laser beam oscillation are summarized in Table I. The procedure for determining these parameters is explained in more detail in Section II–D. The focus position z_f describes the position of the laser focus relative to the workpiece surface in the direction of the z axis. The value $z_f = 0$ means that the focus is located on the surface of the workpieces, a negative value indicates that the focus is positioned within the workpiece, and a positive value that the focus is positioned above the workpiece. Three specimens were prepared for each of the two settings to be tested in tensile tests. No subsequent heat treatment of the welded workpieces was performed.

B. *Evaluation of Mechanical Properties and Microstructure*

To determine the tensile strength of the welded specimens, a universal tensile test machine type Z100 TEW (manufacturer: ZwickRoell) with a load cell for a maximum force of 2500 N was used. The specimens

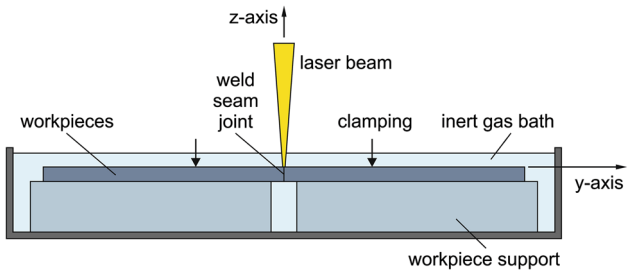

Fig. 1—Experimental setup for welding (schematic).

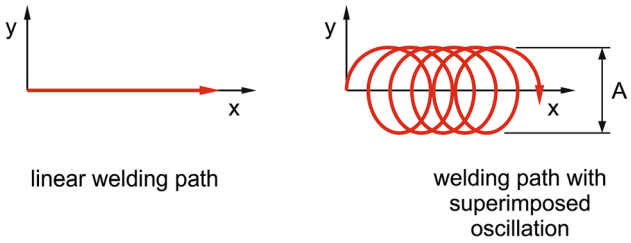

Fig. 2—Comparison of different types of welding paths.

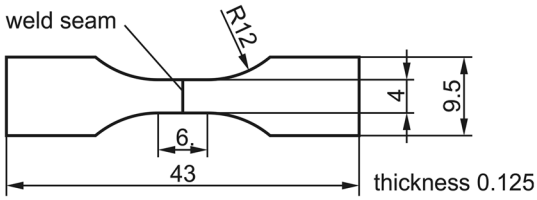

Fig. 3—Dimensions of specimens for tensile tests.

Table I. Selected Parameter for Laser Welding

	P (W)	v (mm/s)	z_f (mm)	A (mm)	f (Hz)
Welding with Superimposed Oscillation (OW)	40	24	0	0.1	300
Linear Welding Path (LW)	40	24	0	0	0

were loaded under a quasi-static tensile stress with a movement speed of 0.5 mm/min until fracture and forces and displacement were recorded.

The welded and tested tensile specimens were then cut longitudinally along the center and bonded with epoxy adhesive between a glass (thickness 100 μm) and a silicon wafer section for the preparation for the ion milling. The edge of this bonded compound was trimmed with 600 grit SiC abrasive paper. A cross-section 2.2 mm long from the weld to the undisturbed specimen area was then processed using the IM5000 ion milling system (manufacturer: Hitachi High-Tech Europe), applying an accelerating voltage of $U_a = 8$ kV, an ionization voltage of $U_i = 2$ kV, and a swing angle of $\pm$ 40 deg over a time of

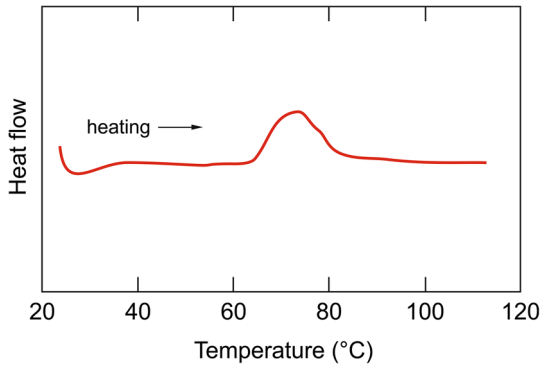

Fig. 4—DSC analysis of the parent material.

105 minutes. For fine polishing, the surfaces were finished over the time of 20 minutes each, first with $U_a = 1$ kV, $U_i = 1.5$ kV, and then with $U_a = 0.7$ kV and $U_i = 1.5$ kV. The observation of the samples prepared in this form was carried out with the scanning electron microscope (SEM) of the type SU5000 (manufacturer: Hitachi High-Tech Europe). This SEM was also used for the fracture surface analysis.

A mapping using energy-dispersive X-ray spectroscopy (EDX) was conducted for selected areas of the ion milled samples using the above SEM in conjunction with an EDX system (manufacturer: Bruker). The system DSC 200 PC Phoenix (manufacturer: Netzsch-Gerätebau) was applied for Differential Scanning Calorimetry (DSC) analyses.

C. *Base Material of the Weld Specimens*

For the experimental procedure, a Ni–Ti foil in annealed condition with a thickness of 125 μm was used that was composed of 55 wt pct Ni and 45 wt pct Ti. The analysis of the parent material with DSC in the temperature range of 20 °C to 110 °C and a heating rate of 10 K/min exhibited one endothermic peak and showed that the material was in an austenitic state at room temperature, Figure 4. Figure 5 depicts the result of the tensile test of the unwelded base material. A maximum tensile strength of 743 MPa and elongation at break of 47 pct were measured.

D. *Methodology of Applied DoE*

The objective of using DoE in this study was to determine, with the smallest possible number of experimental trials, the optimal parameter set that would lead to the maximum tensile strengths of the laser-welded Ni–Ti specimens also considering oscillation of the laser beam. According to the reviewed literature, the laser power P, the welding speed v, and the focus position z_f have a significant influence on the welding result, *e.g.,* Reference 24. When using superimposed oscillation for welding metallic materials, the amplitude A and frequency f of the oscillation play a crucial role, *e.g.*, Reference 35. A post-welding heat treatment with the temperature T and the holding time t was also included, since Ni–Ti welded joints can exhibit considerable

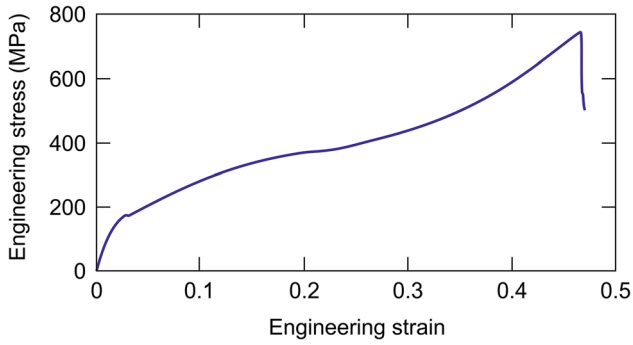

Fig. 5—Stress–strain curve of the parent material.

Table II. Parameter Settings for the Creation of DoE (c: Continuous, d: Discrete)

Parameters	Type	Role	Values
P (W)	ETC	c	30 … 40
v (mm/s)	ETC	c	10.9 … 24
z_f (mm)	ETC	d	− 0.04 | 0 | 0.04
A (mm)	ETC	d	0 | 0.05 | 0.1
f (Hz)	ETC	d	0 | 300 | 1000 | 2000
T (°C)	HTC	d	22 | 150 | 275
t (min)	HTC	d	0 | 10 | 30 | 60

residual stresses,[40] which reduce the tensile strength and which could be relieved by a heat treatment. Table II summarizes the investigated range of parameters applied in the DoE study.

One of the core principles of DoE consists in the randomization of the experimental runs to achieve independence among the results of the tests. This is also one of the factors ensuring that the input–output relationships later discovered by the models are valid at a causal level. However, in some situations it is unfeasible or inconvenient to reset the factor levels between every experimental run, and this is the case for the process parameters governing the post-welding heat treatment applied in this study. From an operational perspective, it is easier to keep T and t fixed for some experimental runs, as this allows the experimenter to apply the same heat treatment to a batch of welded specimens before resetting the process parameters of the oven and proceeding with a new batch. For this reason, a split-plot design[41,42] was selected in which T and t are set as the hard-to-change (HTC) factors that are kept constant for 4 consecutive experimental runs before being reset and proceeding with a new setting of the oven. This also determines the size of the so called "whole plots" within which each easy-to-change (ETC) factor is fully randomized. Figure 6 displays a simplified representation of the complex experimental structure.

Clearly the randomization restrictions described above change the structure of the regression model used to fit the data, as some dependence is potentially created among the samples that belong to the same whole plot. This entails that an appropriate model structure for the data is a mixed model including both fixed and random effects:

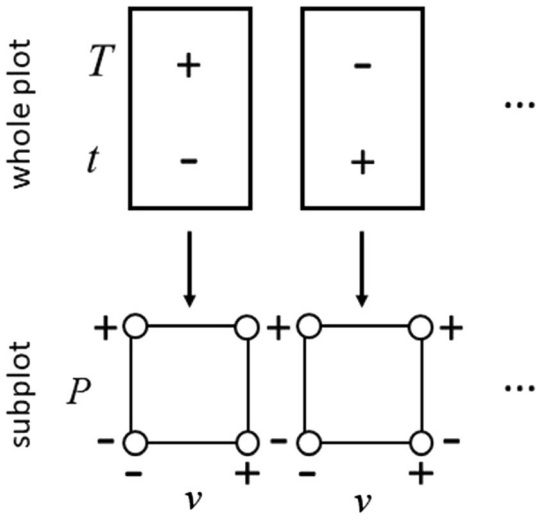

Fig. 6—Simplified framework representing the experimental procedure from a DoE perspective. For readability purposes, only 4 factors of the DoE are shown, and only the low (−) and high (+) levels are considered. While the HTC factors in the whole plots remain fixed, the ETC factors are randomized in the subplots. This generates different error components in the data structure that must be considered in the regression model.

$$\boldsymbol{Y} = \boldsymbol{X\beta} + \boldsymbol{Z\gamma} + \boldsymbol{\varepsilon}, \qquad [1]$$

where $\boldsymbol{Y}$ is the vector of the response observed, $\boldsymbol{X}$ is the known design matrix of fixed effects, that are the ETC subplot effects, $\boldsymbol{\beta}$ is the unknown vector of fixed effects parameters, $\boldsymbol{Z}$ is the known design matrix of random effects, i.e., the HTC whole plot factors, $\boldsymbol{\gamma} \sim N(0, G)$ is the unknown vector of the random effect parameters, and $\boldsymbol{\varepsilon} \sim \mathrm{N}(0, \mathrm{R})$ is the vector of the random error. An appropriate quantification of the variance components G and R is crucial to assess the impact of the randomization restriction on the results of the analysis.

Furthermore, additional complications in generating the experimental design regard the presence of some physical constraints that render some of the input configurations unfeasible. For instance, since one of the study objectives consists in assessing the differences among the OW and LW configurations, one constraint is that if $A = 0$, then also $f = 0$ and *vice versa*, since it is clearly not possible to set a superimposed oscillation characterized by amplitude 0 mm and positive frequency or by a null frequency and positive amplitude. Other constraints regard the T and t of the post-welding heat treatment, as in case T is above the room temperature value (> 22 °C), then t must be at least equal to 10 min, as it is not possible to apply a heat treatment for a null amount of time, and the reverse is also true since if $t > 0$, then T must be at least 150 °C for the heat treatment to be effective. Some preliminary tests also revealed a feasibility range for the ratio P/v that indicates the amount of energy that the material receives per unit of length (J/mm). In order for the weld to be considered at least in principle effective, i.e., the material is connected and does not have holes due to excessive energy received per unit length, the following constraint was imposed when designing the experiment: 1.25 J/mm ≤ P/v ≤ 2.75 J/mm.

One last remark regards the nature of the factors. P and v can be easily controlled during the experiment, and small steps of the factor levels are achievable. For this reason, they are set as continuous factors. On the other hand, the other factors are either more difficult to control or their effect is expected to change only on larger steps of the factor levels, so they are set as discrete, and few levels are selected a priori as reported in Table I.

Overall, the final experimental design developed has 48 runs organized in 12 whole plots. Considering the requirements from the point of view of limited randomization of the trials and the many physical constraints, this can be considered a challenging setting for a DoE application and a relevant case study in the literature.

III. RESULTS AND DISCUSSION

An analysis of variance components of the whole plots (G) and random error (R) is carried out using the restricted maximum likelihood method,[43,44] revealing that the contribution on the overall error imputable to the whole plots is insignificant (0 pct of the total variance). This implies that no dependence is detected within samples that are subjected to the heat treatment in the same batch. For this reason, the random effect can be removed, and the HTC factors can be treated as fixed effects, thus simplifying the model structure.

In the aim of reducing the model complexity by removing nuisance factors, a stepwise backward elimination is carried out to eliminate from the model those effects that are not significant considering a significance level $\alpha = 10$ pct for the statistical test. The results of ANOVA are reported in Table III, whereas the final effects selected, including main effects, interactions, and quadratic effects and related p-values are reported in Figure 7, together with a visualization of the predictive performance of the model developed. Interestingly, many of the most significant effects consist in interactions between main effects. This underlines the importance of DoE in practical applications, as interaction effects are quantifiable only if an appropriate design is constructed for data collection. The final regression model linking the predictors with the response σ_{UTS} is reported in Eq. [2]:

$$\begin{aligned}\sigma_{\mathrm{UTS}} = {} & 724.377 + 2255.117 * A + 0.152 * f - 24.882 * P + 0.085 * T \\ & + 0.235 * t - 37.207 * v \\ & + 498.042 * z_f + 0.004 * T^2 - 28655.795 * z_f^2 - 1.046 * A * f \\ & - 11.533 * A * T \\ & + 0.001 * f * t - 0.007 * f * v + 1.593 * P * v - 0.058 * T * v \\ & - 6.746 * T * z_f \end{aligned} \qquad [2]$$

Figure 8 reports the interaction plots among the factors considered in the experiment. The welding speed v tends to strongly interact with P, f, and T. The

strength of the material increases for high welding speeds and powers, whereas large oscillation frequencies pair best with slower speeds of the laser and the LW configuration interacts favorably with high laser speeds. A post-welding heat treatment operated at high temperatures appears to negatively impact on the ultimate tensile strength σ_{UTS} of the samples if the specimens are welded at high speeds, while the effect is almost negligible for welds operated at slow speeds, even though a minimum value of σ_{UTS} is found for temperatures around 150 °C. In the presence of laser beam oscillation, higher σ_{UTS} is obtained for high frequencies and small amplitudes. Interestingly, the temperature and holding time of the post-welding heat treatment process interact with the amplitude and frequency of the laser beam oscillation, respectively. If the amplitude of oscillation is large, increasing the post-welding annealing temperature has a strong detrimental effect on the performance of the material, whereas if the LW configuration is preferred the effect of the heat treatment temperature is less significant. Applying the heat treatment for prolonged periods has a positive impact on the performance of the material if the sample is welded on a OW configuration at high frequencies, while the impact of the heat treatment time is basically null if the LW configuration is preferred. As the laser focus moves away from the material surface, it is better not to perform the heat treatment at high temperatures.

Figure 9 shows the optimal configuration of the input process parameters according to the model developed, that is the same configuration reported in Table I. Maximal ultimate tensile strength of the material is expected for workpieces that are welded at high P and v of the laser beam, with a superimposed oscillation characterized by $f = 300$ Hz and $A = 0.1$ mm, without any heat treatment after the weld is performed. Figure 10 shows the results for the same configuration when the LW option is preferred.

Figure 11 represents the results of the tensile tests for the specimens welded with the parameters from Table I and Figure 12 summarizes the measured ultimate tensile strengths σ_{UTS}. The determined strengths of the tested specimen ranged between 164 and 308 MPa and were thus significantly lower than the strength of the unwelded specimens with 743 MPa. Nevertheless, it should be underlined that the value of 308 MPa is the highest value registered also considering all the DoE configurations. The OW welds with oscillation of the laser beam showed on average about 5 pct higher strengths than the LW welds without oscillation. However, the OW welds scattered in a wide interval of about 144 MPa, which was about twice as large as the interval of the LW welds with 73 MPa. The elongations at break of the welded specimens were also lower than those of the parent material with 47 pct and were between about 12 and 30 pct for the OW specimens and between about 16 and 27 pct for the LW specimens (Figure 11). This drastic decrease in strength and elongation at break has already been observed in other welds of Ni–Ti foils and was attributed to the brittleness of the material due to the welding process.[22] Also evident in Figure 11 is a deviation of the stress–strain curves of the welded specimens from that of the parent material starting after a comparatively small elongation. Deviations in the stress–strain curves between parent and welded material were observed also for the welding of Ni–Ti wires over a partial section of the curve shortly after the beginning of the load application which was attributed to the increasing local plastic deformation of the weld

Table III. ANOVA Table of the Final Model

Source	DF	Sum of Squares	Mean Square	*F* ratio
Model	16	288,292.60	18,018.3	4.1261
Error	31	135,373.27	4366.9	**Prob > F**
C. Total	47	423,665.87		0.0004*

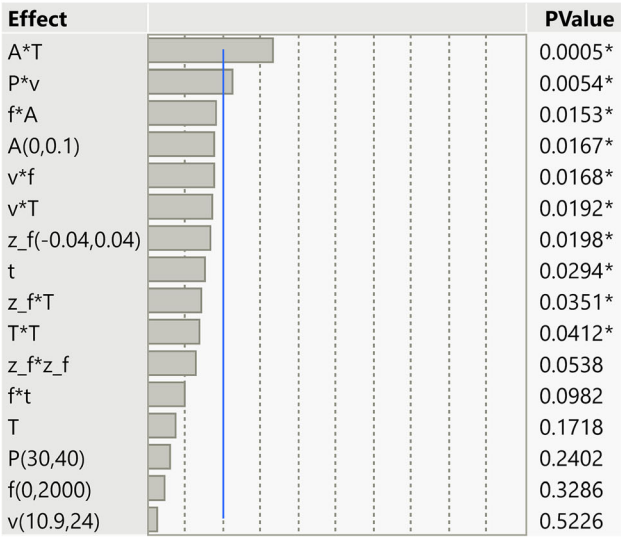

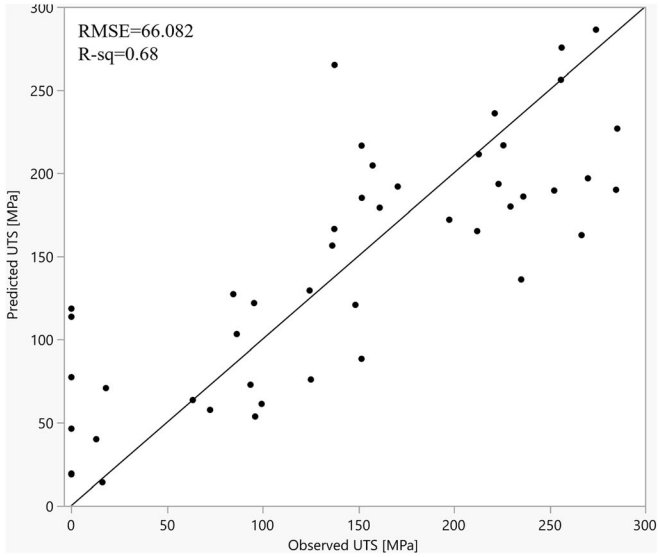

Fig. 7—Significant effects of the regression model used in the DoE analysis (left) and observed *vs* predicted values plot (right).

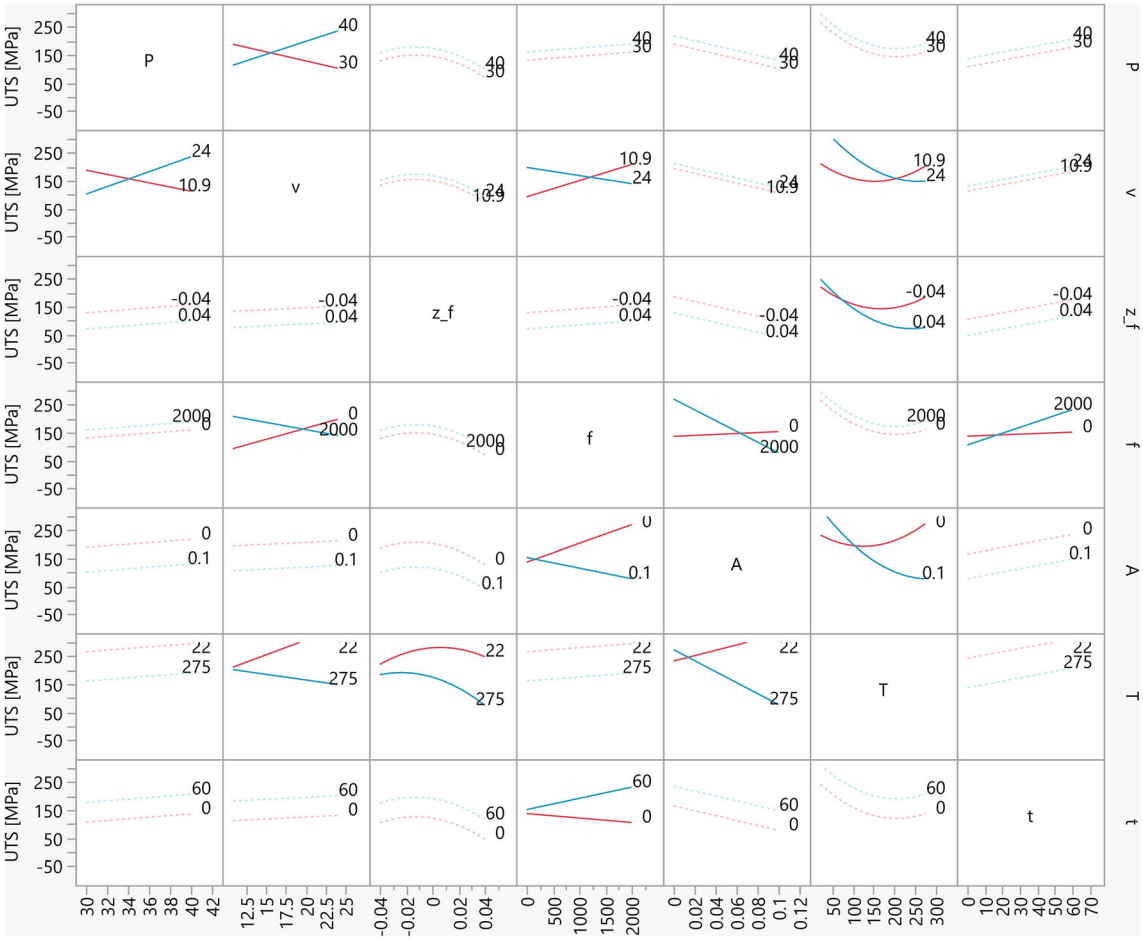

Fig. 8—Interaction plots of the factors considered in the DoE study. Significant interactions are displayed as solid lines, whereas insignificant interactions are displayed as dashed lines.

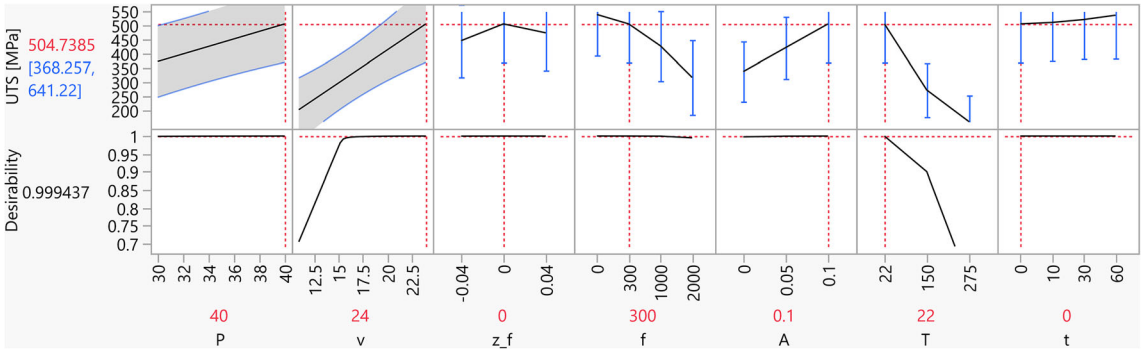

Fig. 9—Optimal OW configuration of the process parameters.

region due to the changes in the microstructural properties as a result of the welding process.[45] It is also noticeable that the stress–strain curves of the OW specimens (samples 1–3 OW in Figure 11) were flatter in the strain range between 1 and 5 pct than the LW specimens (samples 4–6 LW in Figure 11). Also, the curves of the OW specimens were smoother overall in the further course while the LW curves showed fluctuations. These differences in the mechanical behavior of the investigated OW and LW specimens show that the application of an oscillation superimposed on the laser beam movement influences the weld properties. The region in which fracture occurred upon reaching maximum tensile strength was inconsistent, as also indicated in Figure 12, and was in the center of the FZ for some specimens and for some in the border area of the FZ at the transition to the non-melted base material, for both the OW and LW specimens.

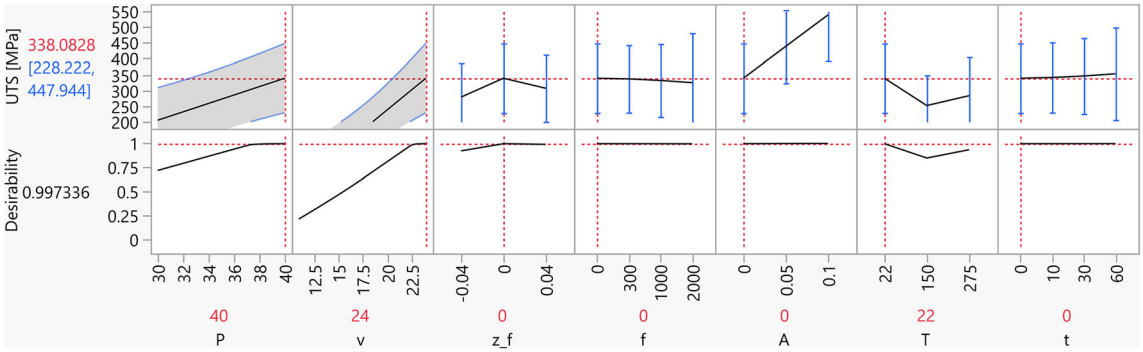

Fig. 10—Optimal LW configuration of the process parameters.

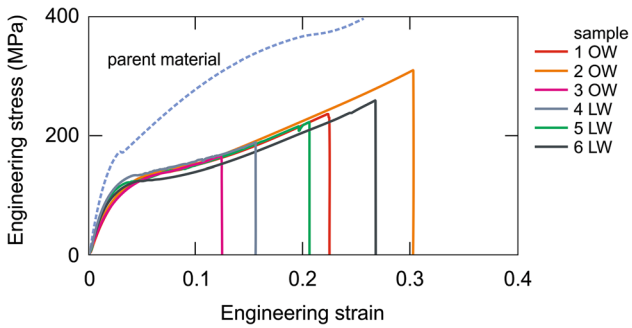

Fig. 11—Stress–strain curves of the laser-welded specimens.

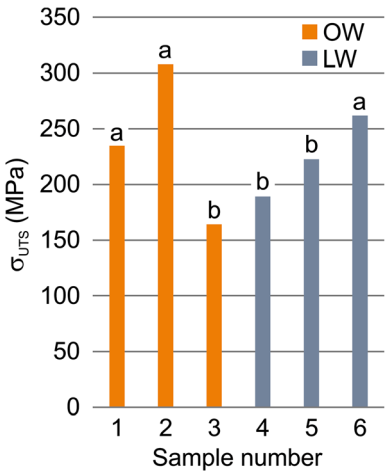

Fig. 12—Tensile strength of samples welded with and without laser beam oscillation (*a* fracture in FZ border, *b* fracture in FZ center).

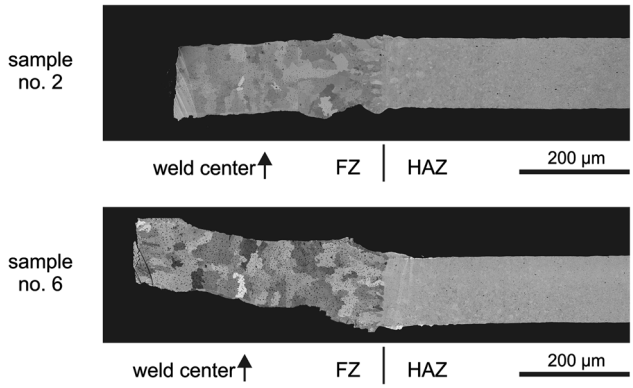

Fig. 13—SEM images of the weld seam after the tensile test for OW sample no. 2 and LW sample no. 6.

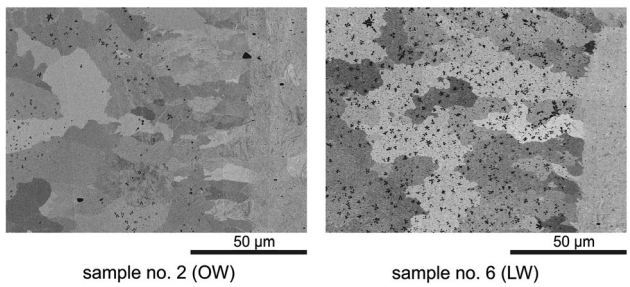

Fig. 14—Detailed view of the microstructure of FZ for OW samples no. 2 and LW sample no. 6.

Figure 13 depicts the weld seam of one half of the specimen after the tensile test for the samples 2 and 6, which resulted in the highest strength value for the OW and LW specimens, respectively. In both cases, the profile of the weld shows a rectangular shape, which is commonly targeted when welding thin foils and occurs at high welding powers and low welding speeds.[29] Horizontal growth of epitaxial, columnar grains is visible at the edge of the FZ due to the accelerated cooling there, with smaller grain size than the vertical grain growth to be seen in the center of the FZ due to the predominant cooling from the direction of the sample surfaces.

Enlarged sections of specimens 2 and 6 in Figure 14 show the material microstructure in the border area of the weld seam. The previously mentioned grain structure of the transition region from FZ to HAZ can be recognized whereby the microstructure of the OW sample no. 2 is slightly finer-grained in the weld than that of the LW sample no. 6. A refinement of the grain size through the use of a superimposed oscillation of the laser beam corresponds to the findings for the laser welding of high-strength steel.[32] At the time the microstructure was analyzed, however, the grain sizes

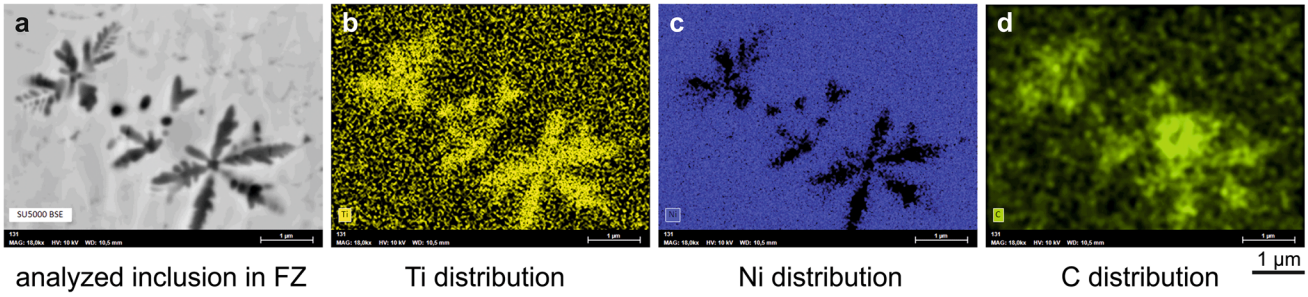

Fig. 15—EDX analysis of inclusions in FZ, (*a*) SEM image, *b–d* distribution of Ti, Ni, and C.

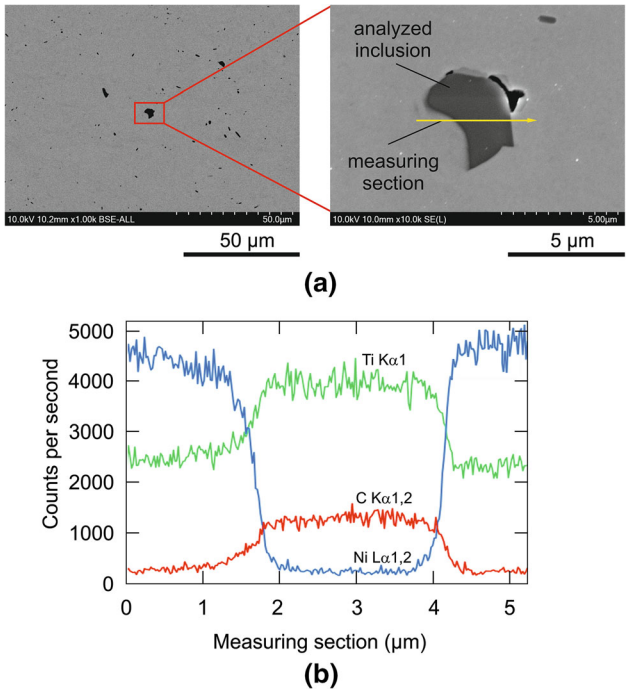

Fig. 16—Titanium–carbon inclusions in the parent material, (*a*) SEM image of parent material and an impurity shown enlarged, (*b*) line scan of material composition.

could not be determined quantitatively due to sample preparation or image evaluation difficulties.

Furthermore, a certain number of inclusions formed in the shape of dark-appearing and branching crystals in the inner part of the grains and at grain boundaries were detected. It is visible in Figure 14 that the number of inclusions is significantly lower in the specimen welded with the application of an oscillating beam movement.

An EDX mapping has shown that the elements Ti and C were particularly strongly represented in these inclusions, while Ni was largely absent (Figure 15). It was therefore concluded that these inclusions were impurities consisting of titanium carbides and resulting from an unanticipated carbon contamination.

As a possible cause for this phenomenon, finely distributed titanium–carbon compounds were found, which were obviously already contained in the parent material and were probably introduced by the manufacturing process of the foil, *e.g.*, by a furnace or tool coating containing graphite. Figure 16(a) depicts for the example of one of the workpieces examined the distribution of these impurities in the parent material, which are visible as black inclusions. While the material surrounding the inclusion consists of the expected chemical composition of the base material, Ti and C were found to be the main elements of the inclusion (Figure 16(b)). These impurities were found in comparable form in all of the samples tested.

Irrespective of the fact that such impurities in the base material are certainly undesirable, the investigations carried out showed that the oscillation of the laser beam appeared to reduce the resulting precipitate-like phenomena in the welding process. The reasons for this remain to be clarified, as slower cooling associated with the superimposed oscillation could promote the formation of precipitations resulting from the impurities. Generally, agitation in the melt bath as induced by beam oscillation would lead to better distribution of the germs and disturb particle growth. It is also known for example from studies on stir casting with strongly agitated bath movement that initially dentritically solidifying nuclei very fast disintegrate into spherical particles contrary to unidirectional solidification[46] which would explain the lower occurrence and the smaller size of crystallized impurities in the weld of the OW sample. Additionally, a remelting of the weld area by the oscillation could promote the diffusion of solute components into the matrix and reduce segregations; a mechanism found in Reference 21 in connection with the reduction of $Ti_4Ni_2O_x$ precipitates by interlayer remelting of a Ni–Ti alloy in an additive manufacturing process. However, further investigations are still necessary here to substantiate these hypotheses.

Figure 17 shows the fracture surfaces of the specimens with the highest and lowest measured tensile strengths of the OW and LW samples. All surfaces show a predominantly brittle fracture behavior. Samples 3 and 4, which fractured in the center region of the FZ at low tensile stresses, are similar and are characterized by recognizable grain structures. There is no immediate difference between specimen 3, which was welded with oscillation of the laser beam, and specimen 4 without oscillation. Samples 2 and 6, each with the highest tensile strength and failure in the border region of the weld, show only partially similar fracture patterns. Sample 2, which was welded with oscillation of the laser beam shows different surface shapes of a brittle

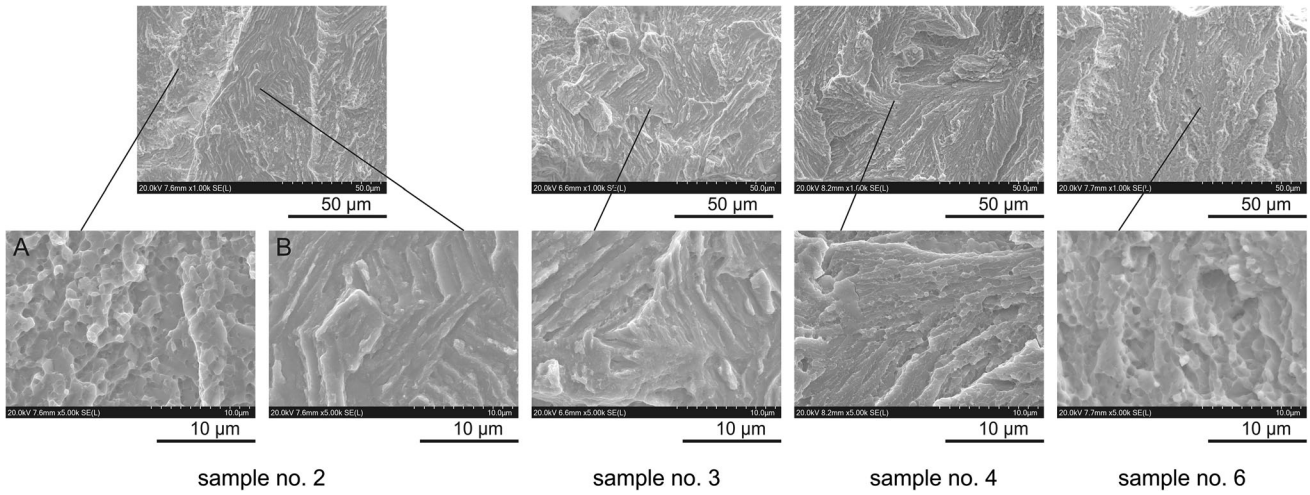

Fig. 17—Fracture surfaces of OW samples no. 2 and 3, and LW samples no. 4 and 6.

fracture (A and B in Figure 17). While fracture pattern A is similar to that of the LW sample 6, fracture pattern B is more comparable to that of samples 3 and 4. It can be assumed that the different fracture surface shapes resulted from differences in the distribution of precipitates or impurities along the grain boundaries, but this remains to be investigated in more detail.

Furthermore, gas inclusions were found in the fracture surfaces of samples 3, 4, and 6, which were particularly pronounced in the LW sample 4. The fact that no (sample 2) or only slight (sample 4) gas inclusions were found in the samples with oscillation supports the finding made by Reference 35 on welds of an Fe–Ni–Co alloy that oscillation contributes to the reduction of pores during welding.

It should also be noted that, as part of the investigations described here, analyses were carried out to measure the transformation temperature of the weld area by means of DSC, which, however, did not yield reliable statements due to the low sample mass of less than half a milligram. There is still a need for further investigation here.

IV. CONCLUSION

The present study has investigated the laser welding of thin films with the thickness of 125 μm made of Ni–Ti alloy. The key results can be summarized as follows:

- With the developed DoE model, based on a split-plot design and the use of the restricted maximum likelihood method, an optimal parameter set for the welding parameters of the Ni–Ti foils could be found as well as the relationships to their interactions. The welding speed v tends to strongly interact with the laser power P, oscillation frequency of the laser beam f, and temperature of post-welding heat treatment T. The tensile strength of the material increases for high v and P, whereas large f pair best with slower v of the laser. Using laser beam oscillation, higher tensile strengths are obtained for high frequencies f and small amplitudes A.
- The tensile tests of samples welded with and without oscillation of the laser beam, using the parameters based on the DoE study, have shown that the welds with oscillation resulted in an approximately 5 pct higher tensile strengths compared to the welds without oscillation. The measured maximum tensile strength value of 308 MPa corresponds with the prediction by the DoE model, but is significantly lower than the tensile strength of the unwelded material and the scatter of the tensile strength values with oscillation are about twice the scatter of the values without oscillation.
- From the material analyses on preparations of the welds processed by ion milling, crystalline titanium carbide inclusions were detected, obviously originating from impurities in the parent material, but their occurrence in the weld was visibly lower when welding with oscillation than when welding without. It is assumed that the oscillation of the laser beam and the resulting repeated heating of the weld seam contribute to a better dissolution of such accumulations in the welded material. Furthermore, it was found that with the oscillation of the laser beam, the occurrence of gas inclusions, which were observed in the center of the weld, was reduced. However, a visible difference in the microstructure with respect to grain size and orientation during welding with and without oscillation could not be detected within the parameters investigated. A largely brittle fracture behavior of all specimens was observed. Certain differences can be seen in the fracture surfaces of the OW and LW specimens when the fracture is located along the border region of the weld.
- Investigations on the transition temperatures in the FZ and HAZ could not be performed on a standard DSC due to the very low mass of the specimens in those areas. Flash-DSC generally working with very small samples could enable the measurements.

The investigations presented here could be carried out on a comparatively small number of samples due to the targeted use of DoE, but thus already provide a number of important scientific results. Topics to be further investigated include the causes of the scatter in tensile strength values and measures to counteract this, more detailed studies of fracture behavior, and the influence of laser beam oscillation on this and on the typical Ni–Ti-based precipitations as well as investigations in simple methods for analyzing the transformation behavior of the welded foil material.

CONFLICT OF INTEREST

On behalf of all authors, the corresponding author states that there is no conflict of interest.

FUNDING

Open Access funding enabled and organized by Projekt DEAL.

OPEN ACCESS

REFERENCES

1. K. Otsuka and X. Ren: *Prog. Mater. Sci.*, 2005, vol. 50, pp. 511–678. https://doi.org/10.1016/j.pmatsci.2004.10.001.
2. H. Holman, M.N. Kavarana, and T.K. Rajab: *Artif. Organs*, 2021, vol. 45, pp. 454–63. https://doi.org/10.1111/aor.13851.
3. S. Rosenthal, F. Maaß, M. Kamaliev, M. Hahn, S. Gies, and A.E. Tekkaya: *Automot. Innov.*, 2020, vol. 3, pp. 195–209. https://doi.org/10.1007/s42154-020-00103-3.
4. G. Costanza and M.E. Tata: *Materials*, 2020, vol. 13, p. 1856. https://doi.org/10.3390/ma13081856.
5. S. Kapuria and H.N. Das: *Ocean Eng.*, 2018, vol. 168, pp. 185–203. https://doi.org/10.1016/j.oceaneng.2018.09.001.
6. S. Zareiea, A.S. Issa, R.J. Seethaler, and A. Zabihollah: *Structures*, 2020, vol. 27, pp. 1535–50. https://doi.org/10.1016/j.istruc.2020.05.058.
7. J.M. McCracken, B.R. Donovan, and T.J. White: *Adv. Mater.*, 2020, vol. 32(20), p. 1906564. https://doi.org/10.1002/adma.201906564.
8. S. Chen, Y. Cao, M. Sarparast, H. Yuan, L. Dong, X. Tan, and C. Cao: *Adv. Mater. Technol.*, 2020, vol. 5(2), p. 1900837. https://doi.org/10.1002/admt.201900837.
9. E.A. Sideris and H.C. de Lange: *Sens. Actuators A*, 2020, vol. 307, p. 111915. https://doi.org/10.1016/j.sna.2020.111915.
10. I. Stachiv, E. Alarcon, and M. Lamac: *Metals*, 2021, vol. 11, p. 415. https://doi.org/10.3390/met11030415.
11. R.A. Abubakar, F. Wang, and L. Wang: *Smart Mater. Struct.*, 2021, vol. 30, p. 013001. https://doi.org/10.1088/1361-665X/abc6b8.
12. Y. Tanaka, Y. Himuro, R. Kainuma, Y. Sutou, T. Omori, and K. Ishida: *Science*, 2010, vol. 327, pp. 1488–90. https://doi.org/10.1126/science.1183169.
13. I. Lopez-Ferreño, T. Breczewski, I. Ruiz-Larrea, A. Lopez-Echarri, M.L. Nó, and J. San Juan: *J. Alloy Compd.*, 2013, vol. 577S, pp. S463–S467. https://doi.org/10.1016/j.jallcom.2012.02.006.
14. J.P. Oliveira, Z. Zeng, S. Berveiller, D. Bouscaud, F.M. Braz Fernandes, R.M. Miranda, and N. Zhou: *Mater. Des.*, 2018, vol. 148, pp. 145–52. https://doi.org/10.1016/j.matdes.2018.03.066.
15. K. Mehta and K. Gupta: *Fabrication and Processing of Shape Memory Alloys*, 1st ed. Springer, Cham, 2019. https://doi.org/10.1007/978-3-319-99307-2.
16. P. Ternik and R. Rudolf: *Int. J. Simul. Model*, 2016, vol. 15, pp. 522–31. http://www.ijsimm.com/Full_Papers/Fulltext2016/text15-3_522-531.pdf.
17. S. Parvizi, S.M. Hashemi, F. Asgarinia, M. Nematollahib, and E. Mohammad: *Prog. Mater. Sci.*, 2021, vol. 117, p. 100739. https://doi.org/10.1016/j.pmatsci.2020.100739.
18. G. Gerstein, C. Kahra, O. Golovko, F. Schäfke, C. Klose, S. Herbst, F. Nürnberger, and H.J. Maier: *Prod. Eng.*, 2021, vol. 15, pp. 271–83. https://doi.org/10.1007/s11740-021-01024-8.
19. B. Li, L. Wang, B. Wang, D. Li, J.P. Oliveira, R. Cui, J. Yu, L. Luo, R. Chen, Y. Su, J. Guo, and H. Fu: *Mater. Sci. Eng. A*, 2022, vol. 843, p. 143135. https://doi.org/10.1016/j.msea.2022.143135.
20. W.C. Ke, J.P. Oliveira, B.Q. Cong, S.S. Ao, Z.W. Qi, B. Peng, and Z. Zeng: *Addit. Manuf.*, 2022, vol. 50, p. 102513. https://doi.org/10.1016/j.addma.2021.102513.
21. B. Li, L. Wang, B. Wang, D. Li, J.P. Oliveira, R. Cui, J. Yu, L. Luo, R. Chen, Y. Su, J. Guo, and H. Fu: *Mater. Des.*, 2022, vol. 220, p. 110886. https://doi.org/10.1016/j.matdes.2022.110886.
22. S. Datta, M.S. Raza, P. Saha, and D.K. Pratihar: *Mater. Manuf. Process.*, 2019, vol. 34, pp. 648–59. https://doi.org/10.1080/10426914.2019.1566608.
23. J.P. Oliveira, R.M. Miranda, and F.M. Braz Fernandes: *Prog. Mater. Sci.*, 2017, vol. 88, pp. 412–66. https://doi.org/10.1016/j.pmatsci.2017.04.008.
24. S. Datta, M.S. Raza, A.K. Das, P. Saha, and D.K. Pratihar: *Opt. Laser Technol.*, 2020, vol. 124, p. 105982. https://doi.org/10.1016/j.optlastec.2019.105982.
25. M. Mehrpouya, A. Gisario, and M. Elahinia: *J. Manuf. Process.*, 2018, vol. 31, pp. 162–86. https://doi.org/10.1016/j.jmapro.2017.11.011.
26. A.R. Razali and Y. Qin: *Procedia Eng.*, 2013, vol. 53, pp. 665–72. https://doi.org/10.1016/j.proeng.2013.02.086.
27. C.J.C. Vertegaal, M.J. Bentum and H.R. Pourshaghaghi: *15th European Conference on Antennas and Propagation (EuCAP) Dusseldorf, Germany, 22–26 March 2021*, IEEE, New York, USA, 2021. https://ieeexplore.ieee.org/document/9411188.
28. M. Garcés-Schröder, T. Zimmermann, C. Siemers, M. Leester-Schädel, M. Böl, and A. Dietzel: *J. Microelectromech. Syst.*, 2018, vol. 28, pp. 869–81. https://ieeexplore.ieee.org/document/8820142.
29. C.W. Chan, H.C. Man, and T.M. Yue: *Metall. Mater. Trans. A*, 2011, vol. 42A, pp. 2264–70. https://doi.org/10.1007/s11661-011-0623-1.

30. M.I. Khan, S.K. Panda, and Y. Zhou: *Mater. Trans.*, 2008, vol. 49(11), pp. 2702–08. https://doi.org/10.2320/matertrans.MRA2008243.
31. J.P. Oliveira, F.M. Braz Fernandes, R.M. Miranda, and N. Schell: *Shap. Mem. Superelasticity*, 2016, vol. 2, pp. 114–20. https://doi.org/10.1007/s40830-016-0058-z.
32. C. Chen, H. Zhou, C. Wang, L. Liu, Y. Zhang, and K. Zhang: *J. Manuf. Process.*, 2021, vol. 21, pp. 761–69. https://doi.org/10.1016/j.jmapro.2021.06.004.
33. Z. Tan, B. Pang, J.P. Oliveira, L. Chen, X. Bu, Z. Wang, B. Cong, and Z. Zeng: *Opt. Laser Technol.*, 2022, vol. 149, p. 107909. https://doi.org/10.1016/j.optlastec.2022.107909.
34. L. Wang, M. Gao, and Z. Hao: *Int. J. Heat Mass Transfer*, 2020, vol. 151, p. 119467. https://doi.org/10.1016/j.ijheatmasstransfer.2020.119467.
35. C. Hu, Z. Zhu, and C. Wang: *J. Mater. Res. Technol.*, 2022, vol. 17, pp. 1259–73. https://doi.org/10.1016/j.jmrt.2022.01.108.
36. W. Ke, X. Bu, J.P. Oliveira, W.G. Xu, Z. Wang, and Z. Zeng: *Opt. Laser Technol.*, 2021, vol. 149, p. 106540. https://doi.org/10.1016/j.optlastec.2020.106540.
37. X. Zhou, H. Zhao, F. Liu, B. Yang, B. Xu, B. Chen, and C. Tang: *Opt. Laser Technol.*, 2021, vol. 144, p. 107389. https://doi.org/10.1016/j.optlastec.2021.107389.
38. J. Hensel, M. Köhler, L. Uhlenberg, J. Dinize Castro, K. Dilger, M. Faß, and J. Baumgartner: *Weld. World*, 2020, https://doi.org/10.1007/s40194-022-01306-4.
39. J.P. Oliveira, R.M. Miranda, N. Schell, and F.M. Braz Fernandes: *Int. J. Fatigue*, 2016, vol. 83, pp. 195–200. https://doi.org/10.1016/j.ijfatigue.2015.10.013.
40. J.P. Oliveira, F.M. Braz Fernandes, R.M. Miranda, N. Schell, and J.L. Ocaña: *Mater. Des.*, 2016, vol. 100, pp. 180–87. https://doi.org/10.1016/j.matdes.2016.03.137.
41. D.C. Montgomery: *Design and Analysis of Experiments*, Wiley, Hoboken, 2017.
42. S.M. Kowalski, P.A. Parker and G.G. Vining: *Qual. Eng.*, 2007, vol. 19, pp. 1–5. https://doi.org/10.1080/08982110601057179.
43. H. D. Patterson and R. Thompson: Maximum Likelihood Estimation of Components of Variance. 1974, In Proceedings of the *Eighth International Biometric Conference*, pp. 197–207.
44. S.R. Searle, G. Casella, and C.E. McCulloch: *Variance Components*, Wiley, Hoboken, 1992.
45. C.W. Chan, H.C. Man, and T.M. Yue: *Lasers Eng.*, 2015, vol. 30, pp. 1–9. http://www.oldcitypublishing.com/journals/lie-home/lie-issue-contents/lie-volume-30-number-3-4-2015/lie-30-3-4-p-247-265.
46. R.J. Smeulders, F.H. Mischgofsky, and H.J. Frankena: *J. Cryst. Growth*, 1986, vol. 76, pp. 151–69. https://doi.org/10.1016/0022-0248(86)90021-7.